

Feature Space Saturation during Training

Justin Shenk^{1*}, Mats L. Richter^{2,3*}, Wolf Byttner⁴, Anders Arpteg⁵, Mikael Huss⁶

¹VisioLab ²University of Osnabrueck ³AIM Agile IT Management

⁴Rapid Health ⁵Peltarion ⁶Codon Consulting

shenkjustin@gmail.com matrichter@uos.de

Abstract

We propose layer saturation - a simple, online-computable method for analyzing the information processing in neural networks. First, we show that a layer's output can be restricted to the eigenspace of its variance matrix without performance loss. We propose a computationally lightweight method for approximating the variance matrix during training. From the dimension of its lossless eigenspace we derive *layer saturation* - the ratio between the eigenspace dimension and layer width. We show that saturation seems to indicate which layers contribute to network performance. We demonstrate how to alter layer saturation in a neural network by changing network depth, filter sizes and input resolution. Furthermore we show that well chosen input resolution increases network performance by distributing the inference process more evenly across the network.

1 Introduction

In recent years various techniques have been proposed for exploring the properties of neural network layers. Understanding how neural networks process information and how this processing may be influenced is vital for designing more efficient and better performing neural architectures. The works of [Zeiler and Fergus \(2014\)](#), [Zhang et al. \(2016\)](#) and [Yosinski et al. \(2014\)](#) are examples of experimental work that show the boundaries and limits of generalization and transferability of features. Recent works by [Raghu et al. \(2017\)](#) and [Alain and Bengio \(2016\)](#) propose techniques that allow for a deeper analysis of networks on a layer wise level.

The common problem with these and other techniques for analyzing the properties of neural networks is their complexity and computational inefficiency, which makes them impractical to use in neural architecture development or in more quantitative studies ([Alain and Bengio, 2016](#); [Raghu et al., 2017](#); [Zhou et al., 2016](#)).

This work shows that a simple on-line computable property, like the covariance matrix of the layer outputs, is able to give interesting insights into the dynamics of the inference process. To enable practical application we provide a technique to efficiently compute the covariance matrix. We show that we can use PCA to project the output of all layers into low dimensional spaces while not negatively affecting predictive performance. We refer to these subspaces as *lossless eigenspaces*.

Based on these findings, we derive *saturation* as a metric for analyzing the dynamics of the inference process. Similar to [Alain and Bengio \(2016\)](#), saturation can be thought of as a level indicator or thermometer, showing the complexity of the processing in the respective layers. By analyzing the distribution of saturation in a model, we show that input resolution is playing a significant role in distributing the inference process among the layers. Based on these findings we are able to provide examples of pathological saturation distribution patterns that indicate mismatches between input resolution and neural architecture.

*Equal contribution.

2 Related work

Works like [Keskar et al. \(2016\)](#) and [Novak et al. \(2018\)](#) focus on analyzing the stability and robustness of converged solutions. A more graphical approach to this topics was made by [Li et al. \(2018\)](#), who visualize the error surfaces near the converged optimum. They also show how architectural properties like skip connections influence the shape of the error surface.

Other publications like [Zhou et al. \(2016\)](#) or [Raghu et al. \(2017\)](#) focus more on the inner workings of neural networks by analyzing the properties of hidden layers as well. For instance SVCCA by [Raghu et al. \(2017\)](#) enables the comparison of two different networks. Similar to our method, SVCCA builds on singular value decomposition and variance-thresholded pruning of eigendirections. However, our proposed saturation metric is conceptually closer to Probe Classifiers for analyzing neural network layers by [Alain and Bengio \(2016\)](#). Probes Classifiers are Logistic Regression models trained on the output of hidden layers, which allow a layer-by-layer analysis of the inference dynamics. Based on their findings [Alain and Bengio \(2016\)](#) also provide examples of symptomatic behavior of sub-optimal architecture design. Another important inspiration for this paper is [Montavon et al. \(2010\)](#), which uses kernel PCA with radial basis functions as well as linear classifiers for their analysis. The authors demonstrate among other things the growing abstraction of features in deeper layers.

A pruning technique has been developed using PCA of hidden layers ([Garg et al., 2018](#)). This technique as well as the followup work by [Chakraborty et al. \(2019\)](#) uses PCA to detect irrelevant layers and filters for pruning and binarization. Investigation of the EfficientNet ([Tan and Le, 2019](#)) architecture provides a useful approach for balancing input resolution, number of filters and number of layers in order to effectively upscale a deep convolutional neural network.

Several of the authors previously proposed saturation as a concept ([Shen et al., 2019](#)), however, we have substantially reworked the computation and explored the theoretical foundation in this work.

3 Layer eigenspaces

3.1 Computing variance eigenspaces and the lossless eigenspaces

We apply PCA on the layer output to determine the eigenspace of the layer's features. Then we sum the largest eigenvalues that explain δ of the layer output variance. The space spanned by these eigenvectors is the variance eigenspace. In this way, we find candidate eigenspaces for the layer. This process is described in section 3.2.

We establish that the layer's output is contained in the eigenspace as follows. We project all validation set output vectors into the space and determine whether the network's validation performance changes. To do this we add special projection layers that only change the output at validation time. This we call a *projected network*. We then apply Student's *t*-test to determine if the network validation performance difference between the projected and the normal network is statistically significant. We pick the smallest δ such that there is not a statistically significant difference. The details are in section 3.3. We refer to the eigenspaces of projected networks with no statistically significant changes in performance as *lossless eigenspaces*.

3.2 Finding layer eigenspaces

In this section we are interested in finding a subspace of the layer output space to which we can restrict layer output vectors $z_{l,i}$ without changing the network's validation performance. We use PCA on the layer output matrix $A_l := (z_{l,1}, \dots, z_{l,n})$ of n samples at training time, thus $A_l \in \mathbb{R}^{n \times w}$ where w is the layer width. To do this efficiently, we compute the covariance matrix $Q(Z_l, Z_l)$, where $Z_l := \sum_{i=1}^n (z_{l,i})/n$, using the covariance approximation algorithm between two random variables X and Y with n samples:

$$Q(X, Y) = \frac{\sum_{i=1}^n x_i y_i}{n} - \frac{(\sum_{i=1}^n x_i)(\sum_{i=1}^n y_i)}{n^2} \quad (1)$$

We make this computation more efficient by exploiting the shape of the layer output matrix A_l : We compute $\sum_{i=1}^n x_i y_i$ for all feature combinations in layer l by calculating the running squares

$\sum_{b=0}^B A_{l,b}^T A_{l,b}$ of the batch output matrices $A_{l,b}$ where $b \in \{0, \dots, B-1\}$ for B batches. We replace $\frac{(\sum_{i=1}^n x_i)(\sum_{i=1}^n y_i)}{n^2}$ by the outer product $\bar{A}_l \otimes \bar{A}_l$ of the sample mean \bar{A}_l . This is the running sum of all outputs $z_{l,k}$, where $k \in \{0, \dots, n\}$ at training time, divided by the total number of training samples n . The final formula for covariance approximation is then:

$$Q(Z_l, Z_l) = \frac{\sum_{b=0}^B A_{l,b}^T A_{l,b}}{n} - (\bar{A}_l \otimes \bar{A}_l) \quad (2)$$

Since we only store the sum of squares, the running mean and the number of observed samples, we require constant memory and computation is done batch-wise. The algorithm requires roughly the same number of computations as the processing of a forward pass does; thus we compute saturation after every epoch. The variables are reset at the beginning of each epoch to minimize the bias induced by weight updates during training.

In convolutional layers, we treat every kernel position as an individual observation.¹ The advantage of this strategy is that no information is lost, while keeping Q at a manageable size. This strategy was proposed by [Raghu et al. \(2017\)](#) after their initial publication and [Garg et al. \(2018\)](#), who use it in their PCA-based pruning strategy for CNNs.

To determine the eigenspace E_l^k such that the projection of output vectors $z_{l,i}$ to E_l^k is lossless, we find $k := \arg \max(\frac{\sum \lambda_k}{N}) \leq \delta$ where $\sum \lambda_k$ is the sum of the largest k eigenvalues.² This technique is similar to how [Raghu et al. \(2017\)](#) apply singular value decomposition in SVCCA - that study fixes δ to 99% of the variance. Pruning strategies by [Garg et al. \(2018\)](#) and [Chakraborty et al. \(2019\)](#) settle on δ of 99.9% and 99% respectively.

3.3 Exploring the properties of projected networks

To study the effect of different values for δ we introduce PCA-Layers, inserted between a (linear or convolutional) layer l with weights and subsequent activation functions. At training time PCA-Layers are passthrough layers. At testing time they project samples $z_{l,1}$ to E_l^k based on the covariance matrix computed while training. We multiply the base of E_l^k with its transpose in order to keep the tensor shape consistent.

The resulting projection matrix $P_{E_l^k}$ restricts layer output to the variance eigenspace E_l^k . We project the fully connected layer's output by multiplying the latent representation matrix A_l with $P_{E_l^k}$. For convolutional layers we compute the (1×1) convolution $A_l * \text{vec}(P_{E_l^k})$. The net effect is to turn a dataset problem into a network parameter one; we study the properties of samples by changing the projection parameters.

First, we study how well the eigenspaces are able to maintain the predictive performance of the model compared to random orthonormal subspaces of equal dimensionality. For this we trained 20 different variations of VGG-style networks on CIFAR10 ([Krizhevsky et al., 2010](#)).³ The *relative performance* of a network for a value of δ is the ratio between the test accuracy with enabled and disabled PCA-Layers. We indirectly control the dimensionality of E_l^k with δ , which is set globally for the entire network.

The results in Figure 1 show that the eigenspaces of the layer outputs are able to maintain the information better than equally sized random orthonormal projections. Relative performance given lower values of δ also degrades slower than random projections.

¹This turns an output-tensor of shape (samples \times height \times width \times filters) into a data matrix of shape (samples \cdot height \cdot width \times filters).

²In order to achieve more accurate results on small networks, we treat the threshold as soft. If $\max(\sum \lambda_k) > \delta \leq \max(\sum \lambda_k) + 0.02$ an additional dimension is added. If $\dim E_l^k = 0$, because a single dimension exceeds the δ -threshold, we set $E := \{v_1\}$.

³In order to include networks of different width (filter sizes) and depth (number of layer) we trained VGG[11,13,16,19] as well as variations of all those architectures with filter sizes reduced by a factor of [2,4,8,16]. All models were trained on a batch size of 128 using the Adam optimizer and a learning rate of 0.001 for 30 epochs.

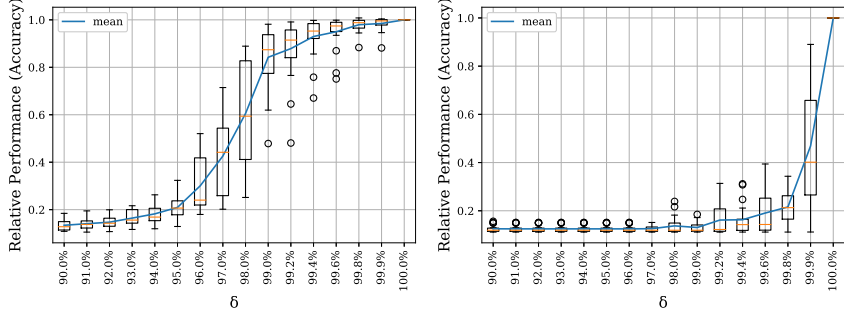


Figure 1: Random orthonormal projections (right) with same dimensionality as E_l^k degrade the performance significantly faster than projections into E_l^k (left).

Next, we explore the upper bounds of this projection by finding a $\delta < 1$ for a trained model such that the difference in predictive performance to the model with disabled PCA-Layers is insignificant. For each network we compare a network’s projected and unprojected CIFAR10 *validation set* performance. We use the eigenspace E_l^k computed during training. We test whether a network’s performance changes relative to the unprojected performance.

Table 1: VGG13 t -statistic, $\mu \neq 0$, selected δ at $\alpha = 0.01$ (n=26). $\mu \neq 0$ in *italics*. Note that at $\delta = 0.996$ the performance difference is insignificant. $\delta = 0.999$ *improves* performance. $\mu_{p-\bar{p}}$ is the average pairwise distance between the test accuracies of unprojected and projected networks.

δ	$\mu_{p-\bar{p}}$	σ	t	p
0.9999	-0.0004	0.0008	-2.42	0.023
0.9998	-0.0005	0.0009	-2.81	0.010
0.999	-0.0017	0.0016	-5.50	0.000
0.998	-0.0017	0.0022	-3.92	0.001
0.996	-0.0005	0.0030	-0.91	0.371
0.994	0.0037	0.0043	4.45	0.000
0.99	0.0178	0.0136	6.68	0.000

Applying Student’s two-tailed t -test to VGG13 (Table 1) shows that at $\delta = 0.996$ we cannot distinguish the projected network from the base network at significance $p = .1$. However, at $\delta = 0.999$, projected network **outperforms** the base network by 0.17% at significance $p = .01$. This means we can **increase** validation performance by **restricting** layer output to a subspace known at training time.

VGG13’s validation performance improves in the range $\delta \in [0.998, 0.9998]$, with a maximum improvement 0.17%.⁴ This shows that there are noisy or not generalizing feature dimensions in the layer output; we use this to develop the concept of *layer saturation* and improve network performance further.

Table 2: VGG19 t -statistic and mean saturation selected δ (n=40). Mean saturation and mean network intrinsic dimension ($\sum \dim E_l^k / n$). The number of dimensions of the entire network is 5860.

δ	t	p	μ_{Sat}	σ_{Sat}	$\sum \dim E_l^k / n$
0.9997	-2.82	0.008	51.2	0.7	2071 ± 93
0.9996	-1.28	0.208	48.8	0.6	1938 ± 88
0.9995	-0.352	0.727	47.1	0.7	1841 ± 86
0.9994	2.18	0.035	45.6	0.7	1766 ± 84
0.9993	2.62	0.012	44.5	0.7	1705 ± 83

⁴The full results are available in the supplementary material.

We also study saturation behaviour in VGG19 (Table 2). At $\delta = 0.9995$, the t -value is insignificant. We need 1841 ± 86 of 5860 dimensions to describe the data. Thus we can **remove** two out of three dimensions without changing network performance.

3.4 Saturation

Since we have shown that variance eigenspaces with sufficiently high δ contain the necessary information for the inference process, we think it is interesting to see how the dimensionality of these spaces given a static δ changes between layers. For this purpose we propose layer saturation:

$$s_l = \frac{\dim E_l^k}{\dim Z_l} \quad (3)$$

Intuitively this *layer saturation* ratio represents the proportion of spatial dimensions occupied by the information in a layer l . Therefore we can think of saturation as a level indicator which shows the fraction of useful dimensions in the output space. We can analyze and compare the inference dynamics of multiple networks by plotting the saturation level of each network layer.

4 Exploring the properties of saturation

We explore the dynamics of the inference process using saturation by training ResNet and VGG-style models on various datasets. We compute the saturation of each convolutional layer of the feed-forward path and plot their saturation levels in the same sequence as the data is propagated through the network. By doing this, we can see how the representation of data is changing from layer to layer, giving us some insight into the inference process.

In all experiments δ is set to 0.99. This particular value was independently used before in similar applications like [Raghu et al. \(2017\)](#), [Garg et al. \(2018\)](#) and [Chakraborty et al. \(2019\)](#) and also yields well interpretable results in our experimental scenarios.

The saturation patterns are computed from the final epoch of training. Probe classifiers are trained on the layer outputs of the model after training concluded.

4.1 Saturation reflects how the inference process is distributed

When looking at the layer saturations along the network structure, we observe in Figure 2 that in some cases a subsequence of layers is a lot more saturated than the rest of the network.

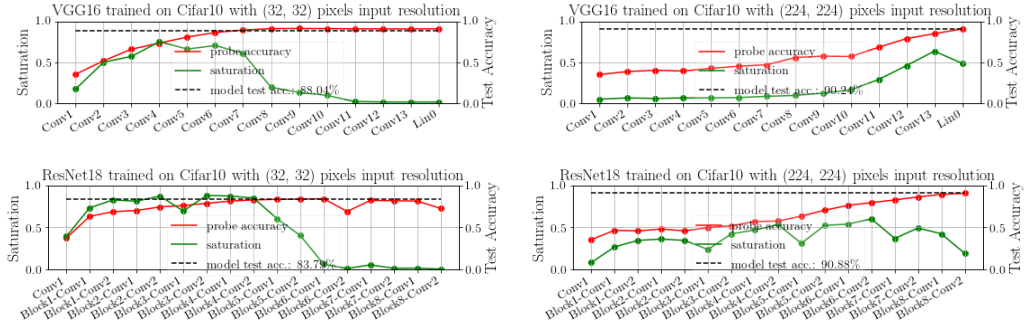


Figure 2: Examples of low saturated subsequences (tails) in trained networks (both left). The probe performance increases only in the highly saturated parts. When the tail is removed by increasing the input resolution (both right) the probe accuracy increases more evenly across all layers.

In order to study this phenomenon, we trained logistic regression probes [Alain and Bengio \(2016\)](#) on each convolutional layer. Probes can be used to observe the progress of the inference by comparing the probe performance to the network performance. We observe in Figure 2 that in some cases the

probe performance is only increasing until halfway through the network's structure - subsequent layers do not contribute.

This is reflected by the saturation pattern. Layers with higher probe performance than preceding layers have high saturation. Layers that do not increase performance, however, have very low saturation. We call this saturation pattern a *tail*.

Based on our observations we define a tail as follows:

A tail is a subsequence of at least 3 consecutive layers in a feed-forward neural architecture with an average saturation at least 50% lower relative to the average saturation of the rest of the network.

This definition is imperfect and does not fit all patterns that we would visually classify as similar to a tail pattern. However, in order to test the implications of the presence of such patterns it is necessary to have a more rigorous definition than purely visual observation.

4.2 Low-saturation ‘tails’

We find that the cause of a tail is generally a mismatch between the depth of the network and input resolution. The impact that input resolution has on the inference dynamics is exemplified in Figure 3. Poorly chosen resolutions result in tails forming in early (too high input resolution) or late (too low input resolution) layers. The result of such a mismatch is reflected in an unevenly distributed inference process among the layers, as shown by the probe classifiers in Figure 3.⁵

Another interesting observation is that the optimal resolution for both architectures seems to be 224×224 pixels, which is the input resolution these architectures were originally designed for [He et al. \(2015\)](#); [Simonyan and Zisserman \(2014\)](#). Furthermore the actual information content encoded in the image seems to be only of secondary concern. CIFAR10 has a native resolution of 32×32 pixels, which means that no information is added by upsampling the images. Despite this, the increase in input resolution has a drastic effect on performance.

We note that an increase of input sizes leads to increased test accuracy. This phenomenon is reproducible on CIFAR10 and TinyImageNet ([Le and Yang, 2015](#)) on all tested architectures.⁶ We compare models trained on the native resolution of the dataset⁷ to the same models trained on images upscaled to 224×224 pixels using bilinear interpolation. The absolute per-model performance increase is 14.3% for CIFAR10 and 10% for TinyImageNet, when removing the tail-pattern by upsampling.

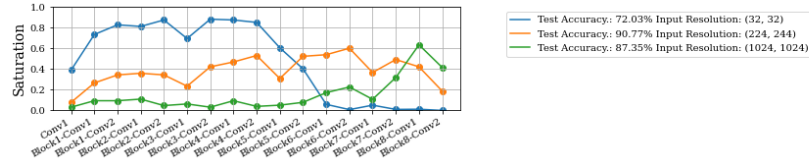


Figure 3: 3 ResNet18 models trained on CIFAR10 on different input resolutions. Too low (32×32) and too high (1024×1024) resolutions result in tail patterns in the front or back of the network. The consequence is decreased performance compared to a better matching resolution like 224×224 in the depicted scenario.

To further test the properties of increased input resolution, we train three ResNet18 models on the Food101 dataset ([Bossard et al., 2014](#)). The first model is trained on Food101 with an input size of 32×32 . The second model is trained on an input size of 224×224 . The third model is trained on images resized to 32×32 pixels and then upscaled again to the input size of 224×224 . By doing this we are able to compare the effects of increased input resolution and the effects of increased input resolution with additional details.

⁵The change in input resolution does not change the number of parameters in the models. Both models feature a global pooling layer, which makes them agnostic to the input resolution.

⁶Resnet[18, 32] and VGG[11,13,16,19] with filter sizes reduced by a factor of 1, 2, 4, 8 and 16.

⁷CIFAR10 has 32×32 , TinyImageNet has 64×64 pixel input resolution.

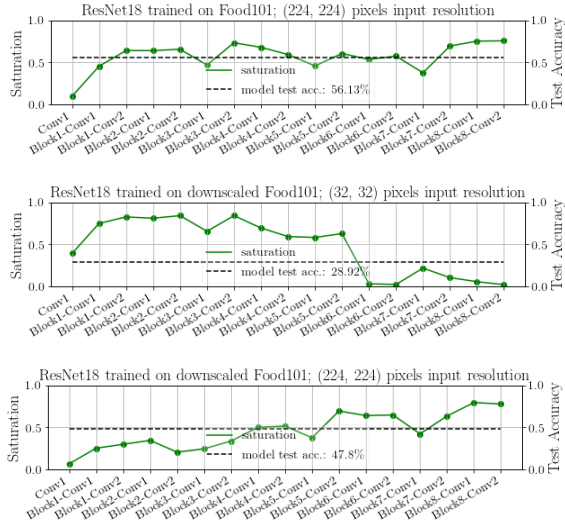


Figure 4: Training ResNet18 on Food101 using different input resolutions. The baseline model is depicted on the top. Low input resolution causes a tail pattern (middle). Upscaling the down-scaled images again to baseline resolution removes the tail and increases performance (bottom).

Figure 4 shows that the behavior is similar to CIFAR10. Increasing the resolution, even if no further details are added to the image, greatly improves performance. In this case performance was increased from 28.9% to 47.8%. Processing the images using the original details resulted in an accuracy of 56.1%. We can thus confirm our observation made on CIFAR10. Even though additional details improve predictive performance, choosing a good input resolution had an even greater impact on the test accuracy in this scenario.

Based on these findings we conclude that the input resolution plays a vital role in controlling how the inference is organized in the network’s structure. This has in turn a significant influence on the generalization performance of the trained model in the scenarios we tested.

4.3 The relation of saturation, filter size and network depth

Since the formation of a tail pattern is the result of a mismatch between input resolution and network architecture, it is also possible to manipulate this saturation pattern by changing the architecture. For example the most straightforward way of changing the length of a tail pattern is changing the number of layers. We focus on the two remaining design axis proposed by [Tan and Le \(2019\)](#), which is the number of layers per network (network depth) and the number of filters per layer (filter size).

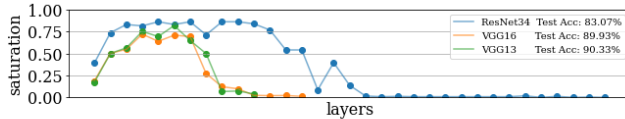


Figure 5: The depth of the network greatly influences the length of the tail pattern, when trained on the same input resolution. The depicted models were trained on CIFAR10 with an input resolution of 32×32 pixels.

The examples from Figure 5 show, that the length of tail pattern depends greatly on the number of layers in a network. Reducing the number of layers is therefore an option to remove the tail. Furthermore it also increases the efficiency of the network since the number of parameters is reduced.

Increasing the filter size in a neural network layer by a fixed scale factor decreases the overall saturation level and vice versa. An example of this can be seen in Figure 6. Changing the filter

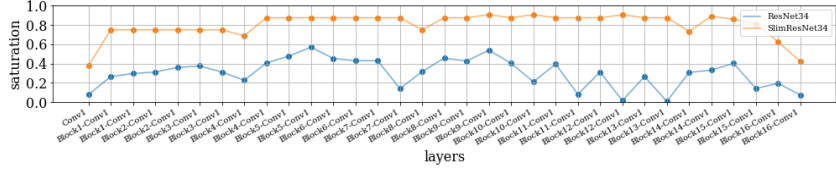


Figure 6: The overall saturation level is increased when the filter size is reduced. In this case the number of filters were reduced by a factor of eight. The models are trained on CIFAR10.

size has only a slight effect on the distribution of the inference process. We find that it is possible, by reducing the number of filters, to spread the inference over more layers. An example of this is depicted in Figure 7. This does not in general lead to improvements in predictive performance. The loss in parameters hurts the performance substantially.

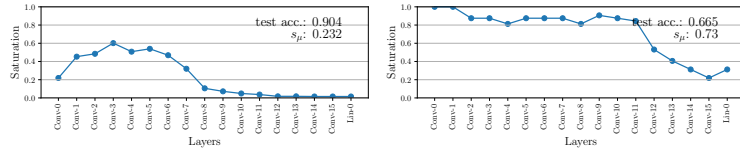


Figure 7: VGG19 trained on 32×32 pixel resolution on CIFAR10 (left), exhibits a tail pattern. Reducing the filter size by a factor 16 (right) has reduced the length of tail and the test performance.

Since the filter size is effectively controlling the dimensionality of the layer output space it is not surprising that the average saturation is greatly influenced by the network width. We explored this relationship by training various VGG-style models on CIFAR10 with altered filter sizes. We observe, as exemplified in Figure 8 that the relationship of the average saturation s_μ with the test performance is logarithmic. This result generally agrees with the intuition of additional parameters yielding diminishing returns.

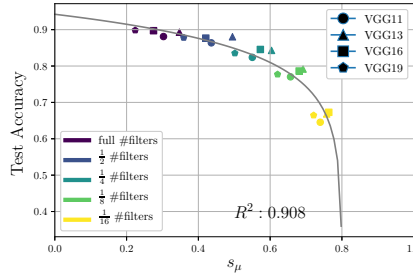


Figure 8: The average saturation s_μ has a logarithmic relation to the test accuracy in these VGG-style models trained on CIFAR10. This relation is mostly influenced by the filter size.

5 Conclusion

In this work we explore the properties of the covariance matrices of neural network layer outputs. We show that it is possible to process the information in a neural network entirely in low dimensional eigenspaces without losing predictive performance.

We introduce the neural network information metric saturation for analyzing the inference dynamics of neural networks at the layer-wise level. By analyzing various networks using saturation and classifier probes we find that high saturated layers contribute more to the quality of the inference. Based on this, we introduce the tail-saturation-pattern, which is a pathological symptom of a mismatch between neural architecture and input resolution. We furthermore provide different approaches to remove the tail patterns by changing the input resolution and the neural architecture and elaborate on the implications on test performance.

Broader Impact

Deep neural networks are powerful but opaque function approximators. Their weight parameters are neither self-evident nor interpretable (Krizhevsky et al., 2012; Zeiler and Fergus, 2013). Neural network architecture design is therefore mostly based on symptomatic analysis; trading predictive performance for computational efficiency. Understanding how networks process information and how this is impacted by network architecture is key to finding more accurate and computationally cheaper designs. We hope that this work contributes to this understanding by giving more insight into the inference dynamics and by providing a computationally cheap diagnostics tool.

This work and the methods used are the indirect result of the limited resources available to our research team. We hope that the techniques described in this work allow other researchers with limited resources to explore the inner workings of neural networks. On a broader scale, we hope that this work contributes to the democratization of neural network research and development by providing further insight and diagnostic tools. This also may enable smaller businesses with talented data scientists to compete against large companies with more (computational) resources at their disposal.

However democratization in this scenario is a double edged sword, since it ultimately means that anyone could be able to develop powerful and efficient deep learning models - regardless of moral and ethical background. This can potentially mean for example better early stage cancer detection and autonomous driving. But on the other hand it might also lead to improved visual targeting systems for rockets or face reidentification systems for large scale targeted surveillance. Not only would democratization make development of all these work ultimately cheaper, but also more broadly available and customizable.

From an environmental point of view, more efficient development and models would decrease the environmental footprint of each individual solution. However, broader scale applications are likely to mitigate this fact or even overshadow it.

References

Guillaume Alain and Yoshua Bengio. Understanding intermediate layers using linear classifier probes. *ArXiv*, abs/1610.01644, 2016.

Lukas Bossard, Matthieu Guillaumin, and Luc Van Gool. Food-101 – mining discriminative components with random forests. In *European Conference on Computer Vision*, 2014.

Indranil Chakraborty, Deboleena Roy, Isha Garg, Aayush Ankit, and Kaushik Roy. PCA-driven hybrid network design for enabling intelligence at the edge. *ArXiv*, abs/1906.01493, 2019.

Isha Garg, Priyadarshini Panda, and Kaushik Roy. A low effort approach to structured CNN design using PCA. *CoRR*, abs/1812.06224, 2018.

Kaiming He, Xiangyu Zhang, Shaoqing Ren, and Jian Sun. Deep residual learning for image recognition. *CoRR*, abs/1512.03385, 2015.

Nitish Shirish Keskar, Dheevatsa Mudigere, Jorge Nocedal, Mikhail Smelyanskiy, and Ping Tak Peter Tang. On large-batch training for deep learning: Generalization gap and sharp minima. *CoRR*, abs/1609.04836, 2016.

Alex Krizhevsky, Vinod Nair, and Geoffrey Hinton. CIFAR-10 (Canadian Institute for Advanced Research). 2010.

Alex Krizhevsky, Ilya Sutskever, and Geoffrey E Hinton. Imagenet classification with deep convolutional neural networks. In F. Pereira, C. J. C. Burges, L. Bottou, and K. Q. Weinberger, editors, *Advances in Neural Information Processing Systems 25*, pages 1097–1105. Curran Associates, Inc., 2012.

Ya Le and Xuan Yang. Tiny ImageNet Visual Recognition Challenge. 2015.

Hao Li, Zheng Xu, Gavin Taylor, Christoph Studer, and Tom Goldstein. Visualizing the loss landscape of neural nets. In S. Bengio, H. Wallach, H. Larochelle, K. Grauman, N. Cesa-Bianchi,

and R. Garnett, editors, *Advances in Neural Information Processing Systems 31*, pages 6389–6399. Curran Associates, Inc., 2018.

Grégoire Montavon, Klaus-Robert Müller, and Mikio L. Braun. Layer-wise analysis of deep networks with gaussian kernels. In J. D. Lafferty, C. K. I. Williams, J. Shawe-Taylor, R. S. Zemel, and A. Culotta, editors, *Advances in Neural Information Processing Systems 23*, pages 1678–1686. Curran Associates, Inc., 2010.

Roman Novak, Yasaman Bahri, Daniel A. Abolafia, Jeffrey Pennington, and Jascha Sohl-Dickstein. Sensitivity and generalization in neural networks: an empirical study. In *International Conference on Learning Representations*, 2018.

Maithra Raghu, Justin Gilmer, Jason Yosinski, and Jascha Sohl-Dickstein. SVCCA: Singular vector canonical correlation analysis for deep learning dynamics and interpretability, 2017.

Justin Shenk, Mats L. Richter, Anders Arpteg, and Mikael Huss. Spectral analysis of latent representations. *CoRR*, abs/1907.08589, 2019. URL <http://arxiv.org/abs/1907.08589>.

Karen Simonyan and Andrew Zisserman. Very deep convolutional networks for large-scale image recognition. *CoRR*, abs/1409.1556, 2014.

Mingxing Tan and Quoc V. Le. Efficientnet: Rethinking model scaling for convolutional neural networks. *CoRR*, abs/1905.11946, 2019.

Jason Yosinski, Jeff Clune, Yoshua Bengio, and Hod Lipson. How transferable are features in deep neural networks? In Z. Ghahramani, M. Welling, C. Cortes, N. D. Lawrence, and K. Q. Weinberger, editors, *Advances in Neural Information Processing Systems 27*, pages 3320–3328. Curran Associates, Inc., 2014.

Matthew D. Zeiler and Rob Fergus. Visualizing and understanding convolutional networks. *CoRR*, abs/1311.2901, 2013.

Matthew D. Zeiler and Rob Fergus. Visualizing and understanding convolutional networks. In David Fleet, Tomas Pajdla, Bernt Schiele, and Tinne Tuytelaars, editors, *Computer Vision – ECCV 2014*, pages 818–833, Cham, 2014. Springer International Publishing. ISBN 978-3-319-10590-1.

Chiyuan Zhang, Samy Bengio, Moritz Hardt, Benjamin Recht, and Oriol Vinyals. Understanding deep learning requires rethinking generalization. *CoRR*, abs/1611.03530, 2016.

B. Zhou, A. Khosla, A. Lapedriza, A. Oliva, and A. Torralba. Learning deep features for discriminative localization. In *2016 IEEE Conference on Computer Vision and Pattern Recognition (CVPR)*, pages 2921–2929, 2016.

A Details on experimental setups

A.1 Details on experimental setups from experiments in section 3.3

A.1.1 Dataset and data augmentation

The experiments are conducted on CIFAR10 (Krizhevsky et al., 2010). The images are channel-wise normalized with $\mu = (0.4914, 0.4822, 0.4465)$ and $\sigma = (0.2023, 0.1994, 0.2010)$. At training time the images are first cropped randomly with a 4 pixel zero-padding on all edges. The size of the crop is 32×32 pixels. Then the crops are horizontally flipped randomly with a probability of 50%. The images of the training set are reshuffled after each epoch.

A.1.2 Models

The experiments use VGG11, 13, 16 and 19 as well as 4 additional variation of the aforementioned architectures. The variations have all filter sizes reduced by a factor of 2, 4, 8 and 16. Furthermore the architectures are slightly modified by adding batch normalization layers after each convolutional layer. In addition the flattening layer serving as the connection between convolution feature extractor and densely connected classifier is replace by a global pooling layer. The variations are included in order to not only include models of various depth but also of varying width in our results. These are two common degrees of freedom in neural architecture design. The modification to the architectures are made in order to include common architectural features that can be considered standard in most modern architectures. Furthermore the global pooling layer makes the models agnostic towards the input resolution. This enables us to alter the input resolution without changing the number of parameters inside the model. PCA-Layers for projecting the network are added after each convolutional and linear layer.

A.1.3 Training setup and parameters

We use the same training setup for all models we test in this chapter. Since we are interested in in-development scenarios, we do not apply hyperparameter optimization. Instead we use default-values of PyTorch wherever possible and otherwise settings that are generally in the common range of hyperparameters used for similar classification tasks. The exact hyperparameter setting are depicted in Table 3. We find that 30 epochs is enough time for all models to converge to a stable solution on CIFAR10.

Table 3: Hyperparameters common to each of the experiments in Section 3.

Parameter	Values
Epochs	30
Batch size	128
Optimizer	ADAM
ADAM: beta1	0.9
ADAM: beta2	0.999
ADAM: epsilon	1e-8
ADAM: learning rate	0.001

A.1.4 Number of experiments conducted

In the experiment in Figure 1 a total of 60 models are trained. Each neural architecture is trained 3 times using the same setup. The experiments in Tables 1 and 2 are repeated 26 and 40 times respectively on the same model using the same setup. We also ran 15 additional experiments on ResNet18 and VGG11, similar to the aforementioned experiments. The results of these are depicted in Table 5 and 8.

A.1.5 Details on PCA-Layer Projections

The eigenvalues and eigenvectors of all PCA-Layers are computed when the switch from training to testing occurs at the end of an epoch. At this point the projection matrix is computed and the

aggregation variables (running sum, running squares and number of seen samples) are reset in each PCA-Layer. The PCA-Layers keep the last computed covariance matrix in memory as an internal variable. This allows us to recompute the projection matrix $P_{E_l^k}$.

A.2 Details on experimental setups from experiments in section 4

A.2.1 Dataset

The experiments conducted in Section 4 are trained on CIFAR10, TinyImageNet and Food101. We additionally reproduce some results on MNIST and TinyImageNet and computed the saturation levels of ResNet18 on ImageNet. These results are not depicted in Section 4, however, these results are included in Appendix B. We chose these datasets in order to test our hypothesis on different levels of complexity, regarding the number of classes as well as the natural resolution of the images.

The preprocessing and data augmentation is the same as in Section 3. The input resolution differs depending on the dataset and the running experiment. If not mentioned otherwise the images are processed in their native resolution. MNIST data is additionally transformed into RGB in order to avoid changes in the neural architecture. In any case, the resizing is performed after the augmentation pipeline is applied on a batch of images.

A.2.2 Models

The experiment uses the same models as in Section 3. Additionally we train ResNet18 and ResNet34 with filter sizes reduced by a factor of 1, 2, 4 and 8. We include the ResNet architectures in order to include another architecture, with a feature (skip connections), that may affect how the information is flowing through the network. We also remove the skip-connections on ResNet18 and 34 for two experiments to observe the effects of disabled skip connections. Different from previously described experiments, none of these architectures have PCA-Layers.

A.2.3 Training setup and parameters

We choose a static training setup of all models and datasets with the same reasoning as in the experiments conducted in chapter 4. Compared to the setup described in Section 3, the batch size is changed to 32 (16 in the cases of ResNet34, VGG16 and VGG19) due to memory limitations. However, we find through brief exploration that slight changes in the hyperparameter optimization described here as well as additional epochs of training do not influence the results described in Section 4 in any meaningful way.

Table 4: Hyperparameters common to each of the experiments in Section 4

Parameter	Values
Epochs	30
Batch size	32 (16 for ResNet34, VGG16 and VGG19)
Optimizer	ADAM
ADAM: beta1	0.9
ADAM: beta2	0.999
ADAM: epsilon	1e-8
ADAM: learning rate	0.001

A.2.4 Probe setup

The data used for training the probes is extracted after the final epoch of training. In case of fully connected layers, the data is simply aggregated and saved as a single data matrix of shape $(samples \times \#neurons)$. In case of convolutional layers this is neither practical nor possible due to limitations in hardware. [Alain and Bengio \(2016\)](#) propose Global Pooling or a random selection of features to bypass this issue. However, we are afraid that global pooling the entire feature map can potentially bias the data and thus the probe performance as a result. In order to mitigate this potential bias we only downsample the feature map to $(4 \times 4 \times \#filters)$ entries using nearest interpolation on the feature map. The reduced feature maps are then flattened into a vector and stored as a data

matrix of shape $(samples \times 4^2 \cdot \#filters)$. We are aware that this method still destroys information. However, by doing this we keep 16 times more dimensions of the original feature space than global pooling. The training test split remains unchanged from the original data. The probes are logistic regression classifiers minimizing cross entropy using the SAGA solver implementation of scikit-learn. The logistic regression is fitted for 100 epochs.

B Additional Results

In this section we present additional results and insights from the experiments presented in section 4.

B.1 Saturation pattern over models and datasets

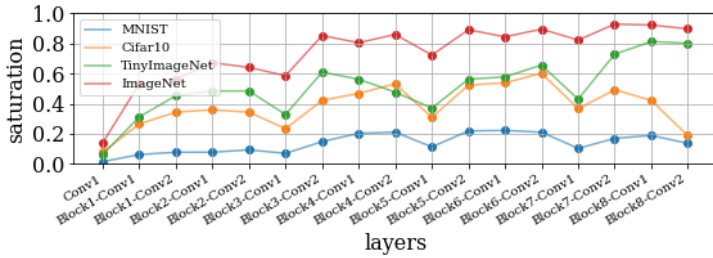


Figure 9: ResNet18 is trained on multiple dataset on a (224×224) input resolution. The overall saturation level increases with problem complexity. MNIST is the simplest problem with binary images and 10 classes, followed by CIFAR10 with slightly larger RGB-image and TinyImageNet with double the resolution compared to CIFAR10 and 200 classes. Finally ImageNet has the highest saturation with 1.000 classes and images of various size and shapes.

B.2 Probe performances and saturation patterns of ResNet18 and 34 with disabled skip-connections trained on CIFAR10

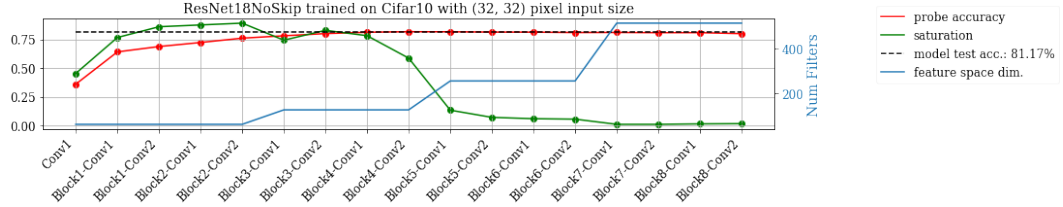


Figure 10:

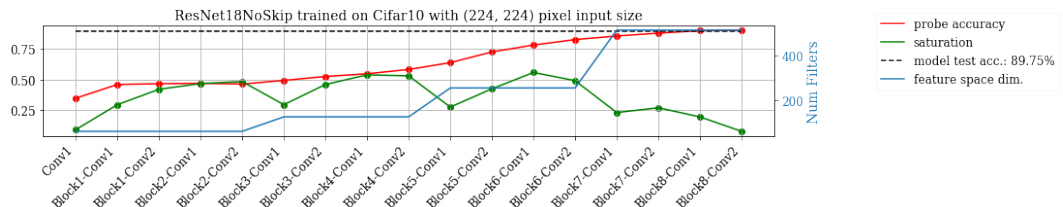


Figure 11:

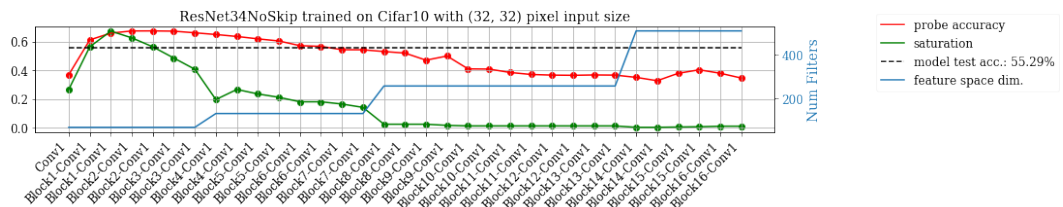


Figure 12:

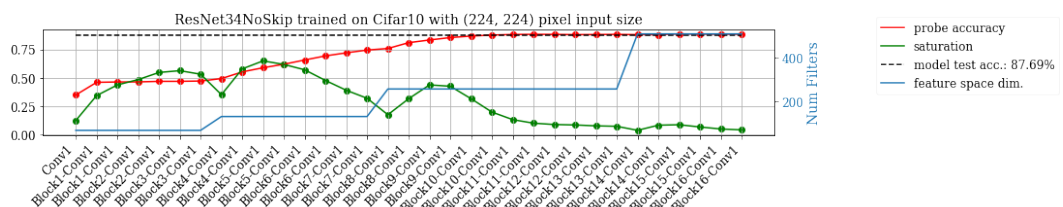


Figure 13:

B.3 Probe performances and saturation patterns for TinyImageNet

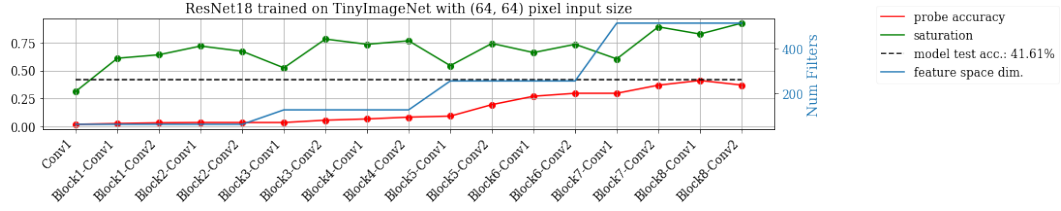


Figure 14:

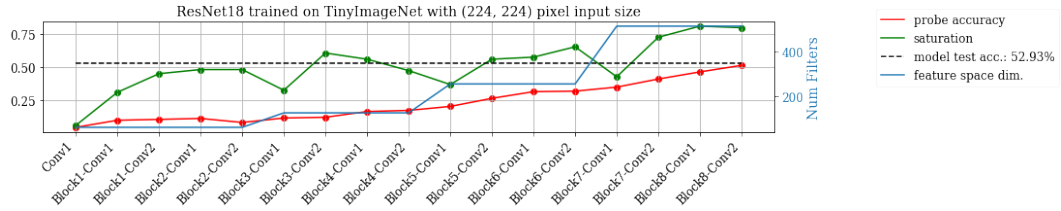


Figure 15:

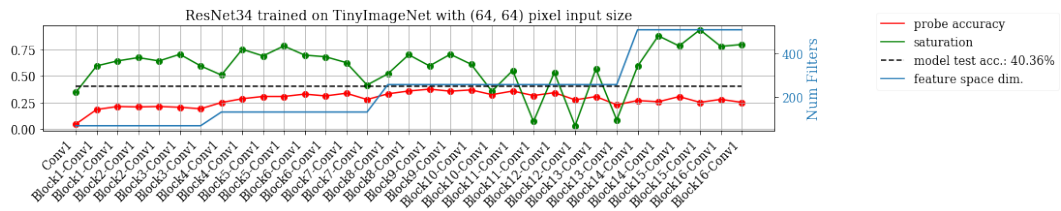


Figure 16:

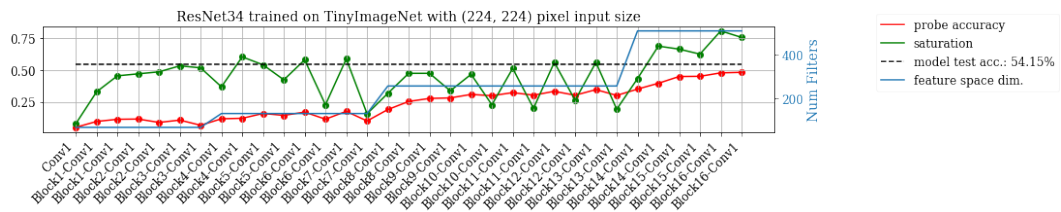


Figure 17:

B.4 Probe performances and saturation patterns for MNIST

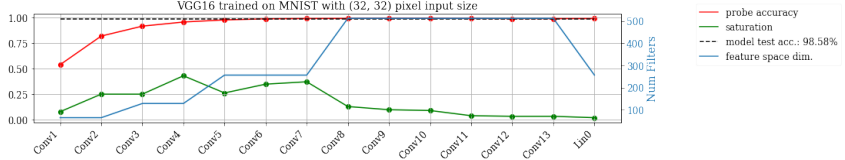


Figure 18:



Figure 19:

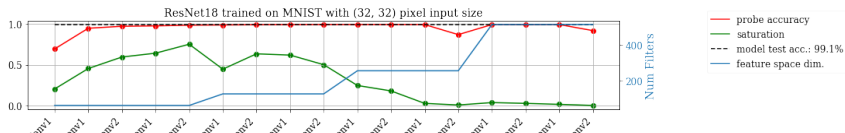


Figure 20:

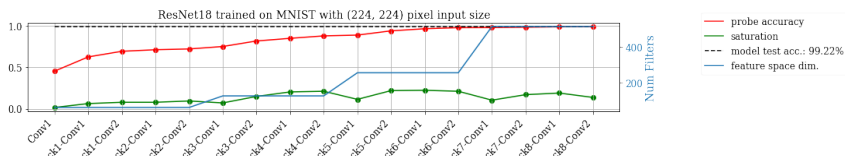


Figure 21:

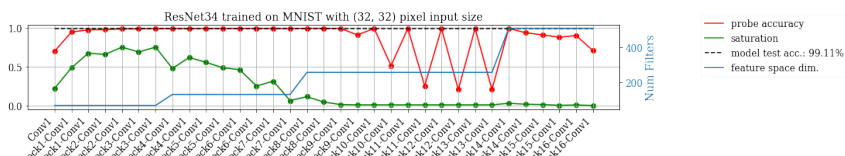


Figure 22:

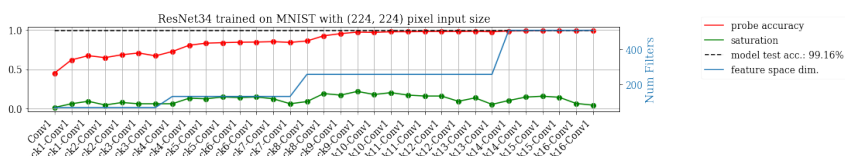


Figure 23:

B.5 Collages of VGG and ResNet-style models

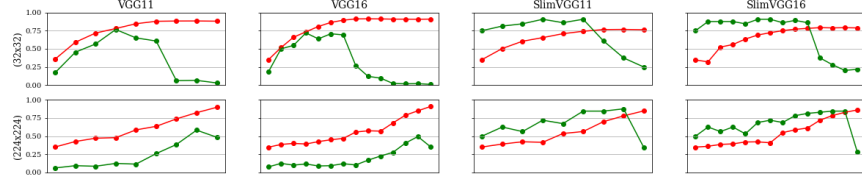


Figure 24: Similar VGG-style models trained on CIFAR10. The models are altered in depth, filter size and input size. Their basic architecture however stays the same. The slim version of the models has all filter sizes reduced by a factor of 8.

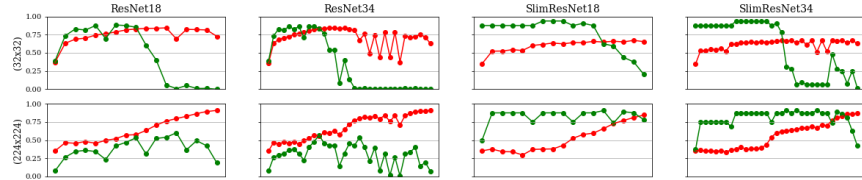


Figure 25: Similar ResNet-style models trained on CIFAR10. The models are altered in depth, filter size and input size. Their basic architecture however stays the same. The slim version of the models has all filter sizes reduced by a factor of 8.

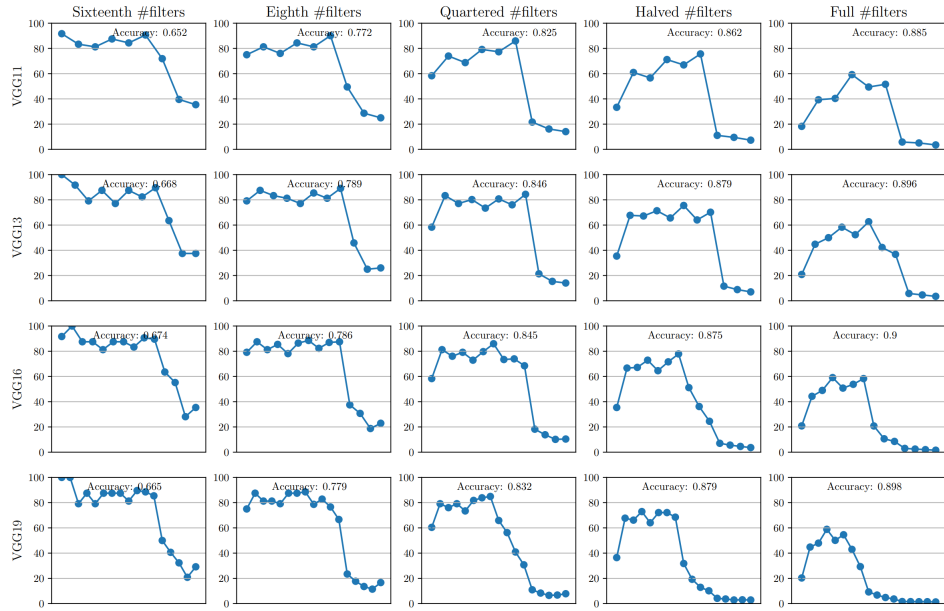


Figure 26: Layer-wise saturation of all tested CNN architectures trained on CIFAR10 for 30 epochs in the configuration for Section 4. The input resolution is (32×32) pixels for all models. The layers are represented on the x-axis in the same sequence as the information is propagated through the network at inference time. The y-axis describes the saturation value. Note the gradual change in the distribution while the number of filters and depth increase.

B.6 Full *t*-Test tables of VGG11, VGG13, VGG16 and ResNet18

Table 5: Sum of projections in VGG11 (n=15). $\mu \neq 0$ (p=.99) in **bold**.

Explained σ	Mean difference	sample σ	t-stat	p-value
0.9999	-0.0001	0.0007	-0.714	0.487
0.9998	-0.0005	0.0008	-2.44	0.029
0.9997	-0.0007	0.0012	-2.07	0.058
0.9996	-0.0005	0.0018	-1.1	0.292
0.9995	-0.0010	0.0018	-2.16	0.049
0.9994	-0.0008	0.0016	-1.8	0.094
0.9993	-0.0010	0.0015	-2.72	0.017
0.9992	-0.0013	0.0014	-3.65	0.003
0.9991	-0.0011	0.0018	-2.51	0.025
0.999	-0.0015	0.0021	-2.74	0.016
0.998	-0.0019	0.0029	-2.49	0.026
0.997	-0.0013	0.0034	-1.46	0.166
0.996	-0.0009	0.0039	-0.888	0.390
0.995	0.0005	0.0037	0.537	0.600
0.994	0.0022	0.0038	2.2	0.045
0.993	0.0056	0.0071	3.03	0.009
0.992	0.0114	0.0110	4.03	0.001
0.99	0.0260	0.0179	5.61	0.000
0.98	0.1073	0.0253	16.4	0.000
0.97	0.2824	0.0954	11.5	0.000
0.96	0.4356	0.0767	22	0.000
0.95	0.5118	0.0616	32.2	0.000
0.94	0.5658	0.0568	38.6	0.000
0.93	0.6385	0.0476	52	0.000
0.92	0.7070	0.0510	53.7	0.000
0.91	0.7574	0.0240	122	0.000
0.9	0.7727	0.0090	333	0.000

Table 6: Sum of projections in VGG13 (n=26). $\mu \neq 0$ ($\alpha = 0.01$) in **bold**.

Explained σ	Mean difference	sample σ	t-stat	p-value
0.9999	-0.0004	0.0008	-2.42	0.023
0.9998	-0.0005	0.0009	-2.81	0.010
0.9997	-0.0010	0.0010	-5.26	0.000
0.9996	-0.0009	0.0010	-4.92	0.000
0.9995	-0.0011	0.0010	-5.46	0.000
0.9994	-0.0012	0.0012	-4.91	0.000
0.9993	-0.0012	0.0012	-4.83	0.000
0.9992	-0.0013	0.0013	-5.17	0.000
0.9991	-0.0016	0.0015	-5.48	0.000
0.999	-0.0017	0.0016	-5.50	0.000
0.998	-0.0017	0.0022	-3.92	0.001
0.996	-0.0005	0.0030	-0.910	0.371
0.994	0.0037	0.0043	4.45	0.000
0.992	0.0096	0.0062	7.91	0.000
0.99	0.0178	0.0136	6.68	0.000
0.98	0.1123	0.0377	15.2	0.000
0.97	0.2254	0.0578	19.9	0.000
0.96	0.4803	0.1022	24.0	0.000
0.95	0.7026	0.0368	97.3	0.000
0.94	0.7536	0.0227	169	0.000
0.93	0.7654	0.0202	193	0.000
0.92	0.7785	0.0164	242	0.000
0.91	0.7867	0.0143	280	0.000
0.9	0.7929	0.0117	345	0.000

Table 7: Sum of projections in VGG19 (n=40). $\mu \neq 0$ (p=.99) in **bold**.

Explained σ	μ_{diff}	σ_{sample}	t-stat	p-value	μ_{Sat}	σ_{Sat}	$\mu(\sum dimE_l^k)$
0.9999	-0.0003	0.0008	-2.65	0.011	60.0	0.6	2613 ± 102
0.9998	-0.0006	0.0011	-3.31	0.002	54.5	0.6	2268 ± 97
0.9997	-0.0006	0.0014	-2.82	0.008	51.2	0.7	2071 ± 93
0.9996	-0.0003	0.0016	-1.28	0.208	48.8	0.6	1938 ± 88
0.9995	-0.0001	0.0017	-0.352	0.727	47.1	0.7	1841 ± 86
0.9994	0.0007	0.0019	2.18	0.035	45.6	0.7	1766 ± 84
0.9993	0.0009	0.0022	2.62	0.012	44.5	0.7	1705 ± 83
0.9992	0.0012	0.0031	2.42	0.020	43.4	0.7	1653 ± 80
0.9991	0.0016	0.0032	3.14	0.003	42.5	0.7	1608 ± 79
0.998	0.0107	0.0148	4.57	0.000	36.0	0.7	1318 ± 73
0.996	0.0771	0.0585	8.33	0.000	30.0	0.7	1074 ± 67
0.994	0.1873	0.0812	14.6	0.000	26.3	0.7	934 ± 62
0.992	0.2754	0.0822	21.2	0.000	23.7	0.6	837 ± 58
0.99	0.3643	0.0900	25.6	0.000	21.8	0.6	765 ± 54
0.98	0.6176	0.0413	94.6	0.000	16.1	0.5	556 ± 41
0.97	0.6559	0.0386	107	0.000	13.1	0.4	451 ± 32
0.96	0.7008	0.0384	115	0.000	11.2	0.3	385 ± 27
0.95	0.7351	0.0337	138	0.000	9.8	0.3	339 ± 24
0.94	0.7550	0.0265	180	0.000	8.8	0.2	303 ± 21
0.93	0.7639	0.0231	209	0.000	7.9	0.2	275 ± 19
0.92	0.7727	0.0167	293	0.000	7.2	0.2	252 ± 17
0.91	0.7775	0.0143	344	0.000	6.6	0.2	233 ± 16
0.9	0.7796	0.0127	387	0.000	6.1	0.2	215 ± 15

Table 8: Sum of projections in ResNet18 (n=15). $\mu \neq 0$ (p=.99) in **bold**.

Explained σ	μ_{diff}	σ_{sample}	t-stat	p-value	μ_{Sat}	σ_{Sat}	$\mu(\sum dimE_l^k)$
1.0	0.0000	0.0000	nan	nan	100.0	0.0	3904 ± 0
0.9999	-0.0002	0.0012	-0.52	0.611	78.5	0.5	2338 ± 87
0.9998	0.0000	0.0013	0.0796	0.938	75.6	0.4	2153 ± 74
0.9997	-0.0002	0.0016	-0.521	0.610	73.9	0.4	2043 ± 67
0.9996	-0.0009	0.0020	-1.66	0.119	72.5	0.4	1963 ± 63
0.9995	-0.0005	0.0022	-0.813	0.430	71.3	0.4	1900 ± 61
0.9994	-0.0006	0.0019	-1.18	0.256	70.4	0.3	1847 ± 57
0.9993	-0.0007	0.0019	-1.48	0.162	69.4	0.4	1802 ± 55
0.9992	-0.0007	0.0022	-1.29	0.217	68.7	0.4	1763 ± 54
0.9991	-0.0006	0.0022	-1.13	0.279	67.9	0.4	1728 ± 52
0.998	0.0031	0.0046	2.63	0.020	62.7	0.3	1493 ± 40
0.996	0.0213	0.0285	2.9	0.012	57.4	0.4	1294 ± 32
0.994	0.0389	0.0454	3.32	0.005	54.0	0.5	1181 ± 28
0.992	0.0579	0.0596	3.76	0.002	51.3	0.5	1100 ± 27
0.99	0.0812	0.0782	4.02	0.001	49.2	0.6	1038 ± 26
0.98	0.1899	0.1042	7.06	0.000	41.7	0.7	841 ± 26
0.97	0.2918	0.1057	10.7	0.000	37.0	0.7	731 ± 26
0.96	0.3649	0.0834	16.9	0.000	33.6	0.6	654 ± 25
0.95	0.4333	0.0757	22.2	0.000	30.9	0.6	595 ± 24
0.94	0.4544	0.0667	26.4	0.000	28.6	0.6	548 ± 24
0.93	0.4787	0.0668	27.7	0.000	26.7	0.6	508 ± 24
0.92	0.4896	0.0638	29.7	0.000	25.1	0.6	475 ± 23
0.91	0.5119	0.0582	34	0.000	23.6	0.6	446 ± 22
0.9	0.5296	0.0574	35.8	0.000	22.4	0.6	421 ± 21

C Further details on complexity and saturation

C.1 Feature map downsampling

The resolution of the feature map has a multiplicative effect on the number of computations required for updating the covariance matrix. Another problem is that the early convolutional layers yield more data points than later layers for computing the covariance matrix, since their feature map is larger. To address both issues we experiment with downsampling the feature maps using nearest interpolation. We find that downsampling feature maps such that the resolution of the feature map never exceed 32×32 pixel did not visibly change the saturation pattern. We did not apply this method in any of the experiments, since we did not explore the biases induced by this method enough. We include this section only to mention that this is a possibility to make computation of saturation more efficient.

C.2 On-line covariance computation and floating point precision

Another issue when on-line computing a covariance matrix is the precision of floating point values. Neural networks are generally processed in full precision. However, for large amounts of data the compounding round-off errors induced by the 32-bit precision of the variables may induce errors. For this reason all computations concerning saturation are performed in double precision. This is also true for the PCA-Layers. Before the update of the covariance matrix is performed, the data is cast in double precision. The running sum, running squares are double precision float arrays as well.

C.3 Effect of eigenspace projections on the reconstruction of a convolutional autoencoder

In order to visualize the effect of projection into the eigenspace we train an autoencoder on the Food101 dataset.

C.3.1 Convolutional autoencoder architecture

Table 9: Convolutional Autoencoder Architecture.

Encoder	Decoder
512 \times 512 \times 3 Input	(3 \times 3) conv, 8 ReLU, same-padding
(3 \times 3) conv, 16 filters, ReLU, same-padding	upsampling, nearest, scale-factor 2
(2 \times 2) max pooling, strides 2	(3 \times 3) conv, 8 filters, ReLU, same-padding
(3 \times 3) conv, 8 filters, ReLU, same-padding	upsampling, nearest, scale-factor 2
(2 \times 2) max pooling, strides 2	(3 \times 3) conv, 16 filters, ReLU, same-padding
(3 \times 3) conv, 8 filters, ReLU, same-padding	upsampling, nearest, scale-factor 2
(2 \times 2) max pooling, strides 2	(3 \times 3) conv, 3 filters, ReLU, same-padding

C.3.2 Hyperparameters

Table 10: Hyperparameters for the convolutional autoencoder.

Parameter	Values
Input Resolution	(224 \times 224)
Epoch	50
Batch size	128
Optimizer	ADAM
ADAM: beta1	0.9
ADAM: beta2	0.999
ADAM: epsilon	1e-8
ADAM: learning rate	0.0001

C.3.3 Reconstruction examples for different values of δ

To test the effects of convolutional and linear projections.

Table 11: Reconstruction examples for different values of δ . PCA is applied on all convolutional layers.

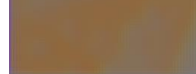
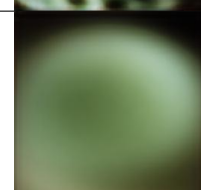
δ	loss	Reconstruction
Original	-	
100%	0.033	
99.9%	0.065	
99.5%	0.089	
99%	0.120	
95%	0.216	
90%	0.234	

Table 12: Reconstruction examples for different values of δ . PCA is applied on the fully connected encoding layer.

δ	$\dim E_{encoding}^k$	loss	Reconstruction
Original	-	-	
100%	8192	0.033	
99.9%	4374	0.035	
99.5%	1332	0.049	
99%	597	0.062	
95%	17	0.148	
90%	1	0.222	